JOURNAL OF AIRCRAFT
Vol. 45, No. 6, November–December 2008

Flight Data Analysis and Simulation of Wind Effects During Aerial Refueling

Atilla Dogan* and Timothy A. Lewis†
University of Texas at Arlington, Arlington, Texas 76019
and
William Blake‡
United States Air Force Research Laboratory, Wright–Patterson Air Force Base, Ohio 45433

DOI: 10.2514/1.36797

This paper presents an analysis of data obtained in an automated aerial refueling test flight conducted with a KC-135 as the tanker and a Learjet 25 as the surrogate receiver unmanned aerial vehicle. The purpose is to identify the wind induced by the tanker wake and its effect on the receiver aircraft. From the available flight data, a direct computation of the winds experienced by the tanker and receiver is carried out. The mean variation of the receiver wind is compared with the tanker wind when the receiver is at the observation and contact positions. This results in the identification of the wake-induced wind. A spectrum analysis is conducted to characterize the turbulence and to identify the pilot effects. The paper also presents methods used to model 1) prevailing wind, 2) wake-vortex-induced wind, and 3) turbulence as the three sources of wind that the aircraft are exposed to and the approach used for incorporating the wind effect into the dynamic simulation of the aircraft. The test flight is simulated in various cases with different turbulence models and flight controllers. The simulation results are analyzed and compared with the flight data in terms of the power spectral densities and mean variations to validate the wind and turbulence modeling techniques.

I. Introduction

THE U.S. Air Force Research Laboratory (AFRL) is currently investigating the feasibility of automated aerial refueling (AAR) of unmanned aerial vehicles (UAVs). This program involves a series of flight tests using a KC-135 tanker and a Learjet 25 as a surrogate for the UAV receiver. During the first flight test, the Learjet was flown by a pilot, without an automatic positioning system. The objectives of the flight test were to 1) verify acceptable handling qualities of the Learjet in the tanker's wake, 2) assess the performance of Global Positioning System (GPS)/electro-optical guidance for determining relative position, and 3) obtain flight data for investigating the wake vortex effect on the Learjet.

In the design, development, and validation of control algorithms for automated aerial refueling, a mathematical model and computer simulation of the receiver dynamics during the refueling are essential. To generate authentic results from the simulation, it is critical to model the receiver aircraft with sufficient accuracy, taking into account all major factors that influence its dynamics. The most significant one of these is the aerodynamic coupling of the receiver with the tanker aircraft through the trailing wake-vortex system. This system generates a nonuniform wind field, which is both deterministic and stochastic, over the receiver aircraft, inducing additional forces and moments. It also reduces the reliability of the receiver airspeed measurement because the measured local airspeed is no longer a true representation of the wind field to which the aircraft is exposed.

Presented at the AIAA Atmospheric Flight Mechanics Conference, Honolulu, HI, 18–21 August 2008; received 23 January 2008; revision received 22 May 2008; accepted for publication 13 June 2008.

*Assistant Professor, Department of Mechanical and Aerospace Engineering. Senior Member AIAA.
†Graduate Student, Department of Mechanical and Aerospace Engineering. Member AIAA.
‡Aerospace Engineer. Associate Fellow AIAA.

Recent work [1–4] has dealt with demonstration of the benefit of and issues with the control system development for aerial refueling. Most of this work treats the vortex as an unknown disturbance or stochastic turbulence in the control law development and validation procedure. Because vortex-induced velocities acting on an aircraft are highly nonuniform, standard aerodynamic force and moment equations, based on airspeed, angles of attack, and sideslip, and uniform wind components and gradients acting at the center of mass of the aircraft cannot be used directly. To overcome this difficulty, two approaches are commonly used [5–7]. The first generates a database of induced forces and moments for a specific pair of aircraft by computational fluid dynamics models or wind-tunnel and/or flight-test measurements. The required databases can be extremely costly to generate, are too computationally intensive to use for even near real-time simulation, and are very difficult to use in control system development. Furthermore, they are specific to certain pairs of aircraft and flight conditions. The second approach is either to completely avoid modeling the effect of nonuniform wind, and model it as an unknown disturbance, or to model it in a simplified manner. A vortex effect modeling technique (VEMT) has recently been developed that enables the use of standard dynamic equations of motion and aerodynamic buildup equations with wind-effect terms included [8–15]. The technique has proven to be very useful and accurate in the case of formation flight modeling and control [8–10,12–14]. It has also been implemented for aerial refueling simulation and control design verification Dogan et al. [16–18] and by other researchers [19].

This paper presents the analysis of the AFRL AAR test flight data for the purpose of characterizing the effect of the wake vortices on the wind field behind the tanker on the dynamic response of the receiver. The analysis is done by extracting, from the flight data, the components of the winds that each aircraft was exposed to in the test flight. The comparison of the mean variation of the wind that the receiver experienced with that experienced by the tanker enables the direct observation of the wind induced by the trailing vortices of the tanker. Spectrum analysis of the wind components is conducted to characterize the turbulence present in the wind experienced by the aircraft. The question whether the turbulence characteristics change in the wake of the tanker is investigated by comparing the power

spectral density functions. Further, power spectral density functions of the acceleration and angular velocity measurements are computed to identify the effect of the pilot on the receiver response. The paper also presents the methods used to simulate the test flight including the wake-vortex-induced wind and turbulence. Comparison of the simulation results with the flight data is used to validate the wind and turbulence modeling techniques.

The paper is organized as follows. Section II presents the methods used to model 1) prevailing wind, 2) wake-vortex-induced wind, and 3) turbulence as the three sources of wind that the aircraft are exposed to, and the approach used for incorporating the wind effect into the dynamic simulation of the aircraft. Section III gives the relevant details of the test flight. In Sec. IV, the true airspeeds of the receiver and tanker are compared. Section V explains the method used to compute the components of the winds experienced by the receiver and tanker, and analyzes the results. Section VI presents the power spectral density analysis of the computed wind components. Section VII summarizes the procedures of simulating the test flight and describes various simulation cases that are run using different turbulence models and flight controllers. Section VIII analyzes the simulation results and compares them with the flight data in terms of the power spectral densities and mean variations. Finally, Sec. IX presents the concluding remarks and topics for future research.

II. Wind Modeling Techniques

During aerial refueling, the wind experienced by the aircraft can be divided into three components. Both the tanker and receiver aircraft are subject to the same prevailing wind present during the flight. Further, both aircraft experience turbulence along with the prevailing wind. In addition to prevailing wind and turbulence, the wind experienced by the receiver is also contributed to by the tanker's wake vortex. The total wind experienced by the tanker is assumed to be the superposition of prevailing wind and turbulence, whereas the wind that the receiver is subject to is modeled as the superposition of prevailing wind, turbulence, and vortex-induced wind. This section presents the methods used to model each wind component.

In this paper, several reference frames will be referred to. The inertial frame is the local x-north, y-east, z-down navigational frame under a nonaccelerating flat Earth assumption. The tanker and the receiver each have an associated body-fixed frame centered at the aircraft center of mass (c.m.), following the common x-forward, y-right, z-down convention used in flight dynamics. The orientation of the body frames are parameterized by the standard 3-2-1 Euler angles (ψ, θ, ϕ): yaw, pitch, and roll. Additionally, each aircraft has a wind frame using the standard angle-of-attack and sideslip angle (α, β) definitions.

A. Prevailing Wind

The prevailing wind is essentially the semisteady weather of the day and can be modeled by any appropriate function. In this paper, one objective is to simulate the test flight, and thus the prevailing wind that the aircraft will be subjected to in the simulation should be the same as that experienced in the actual test flight. Thus, the prevailing wind for the simulation is obtained from the mean variation of the wind that the tanker experienced during the test flight. The calculation of the tanker wind from the test flight data is described in Sec. V. The procedure for the mean variation calculation is given in Sec. VI.

B. Vortex Effect Modeling Technique

Using lifting line theory [20], the wing and the horizontal tail of the tanker aircraft can be modeled as fully rolled-up horseshoe vortices as depicted in Fig. 1. The part of the vortex sheet along the span of the wing or horizontal tail is the bound vortex, whereas the parts that continue in the downstream direction are the trailing or tip vortices [20]. The half-length of a bound vortex, which also determines the origins of the trailing vortices on each side, is $\pi/4$ times the physical half-span. As depicted in Fig. 1, wing vortices rotate inward as the wing generates positive lift, and tail vortices rotate outward as the horizontal tail generates negative lift. The wing vortices are much stronger than the tail vortices as the wing generates more lift; for example, about 34 times more lift by the wings of the tanker in the AAR flight condition. The tip vortices are always aligned with the downstream direction, that is, the air velocity vector. This implies that the tip vortices rotate relative to the body frame of the tanker as the angle of attack and sideslip angle change.

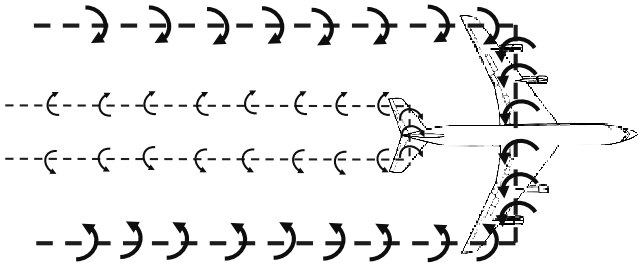

Fig. 1 Depiction of horseshoe vortices for wing and horizontal tail.

The Biot–Savart law [21], along with the modified Helmholtz horseshoe-vortex model [9], computes the magnitude of the wind induced by each filament at a given point as

$$W_r = \frac{\Gamma r}{2\pi(r^2 + r_c^2)}\left[1 - \exp\left(-\frac{r^2}{4\upsilon\tau}\right)\right] \tag{1}$$

where Γ is the vortex strength, r is the radial distance from the point to the filament, r_c is the radius of the vortex core, υ is the viscosity parameter specified [9] as $0.06 \times \Gamma$, and τ is the vortex age specified as the distance to the vortex filament divided by the speed of the tanker [9]. The strength of a vortex filament, including the effect of finite length, is [9,21]

$$\Gamma = \frac{L}{\rho V(\pi/4)b}\frac{\cos\gamma_1 + \cos\gamma_2}{2} \tag{2}$$

where L is the lift generated by the wing or tail, ρ is the air density, V is the airspeed of the tanker, b is the span of the wing or tail, and γ_1 and γ_2 are angles from the endpoints of the filament to the point of interest. Note that γ_1 and γ_2 are always nonzero for bound vortices, whereas either γ_1 or γ_2 is zero for tip vortices, as tip vortices are modeled to be semi-infinite. There are a total of six vortex filaments: a wing-bound vortex, two wing-tip vortices, a tail-bound vortex, and two tail-tip vortices. The velocity of the wind induced by the wake-vortex system of the tanker at a given point is the vector sum from all six filaments.

As the point of interest moves behind the tanker, the vector sum yields a wind velocity vector of different magnitude and direction. Figure 2 illustrates an example on how the induced wind at the origin of the body frame varies as the receiver laterally traverses the tanker's wake. During the lateral move, the receiver is 35.5 m behind and 8.5 m below the tanker (note that the tanker has a wingspan of 39.9 m). The three plots in the figure show the components of the

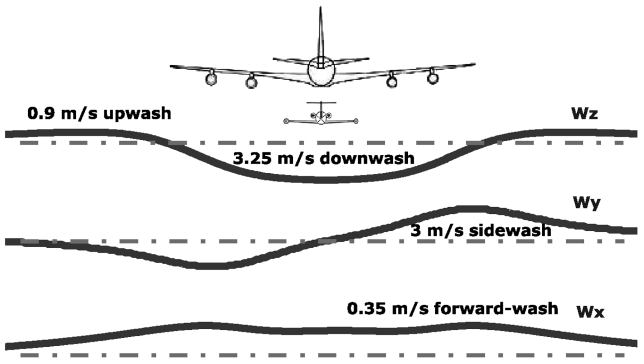

Fig. 2 Example of the nonuniform wind distribution behind the tanker aircraft.

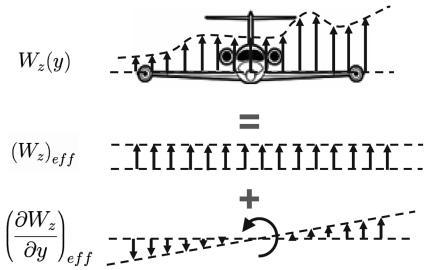

Fig. 3 Nonuniform wind distribution approximated by uniform wind and wind gradient.

wind vector in the body frame of the receiver with the maximum values given in m/s.

Figure 2 also shows that the receiver aircraft may have a significant wind gradient over its span/length/height depending on its position relative to the tanker. A previous paper by Dogan et al. [9] introduced a technique for modeling the effect of a nonuniform wind distribution on the dynamics of an aircraft. Using this technique, a nonuniform wind distribution over an aircraft is approximated by a uniform wind component and a uniform wind gradient. Figure 3 depicts the approach applied to a nonuniform distribution along the y axis of the body frame of the wind component in the body-z direction. As depicted in Fig. 3, the nonuniform $W_z(y)$ is approximated by the effective wind W_z and effective wind gradient $(\partial W_z/\partial y)_{\text{eff}}$. The same approach is used for all three components of the wind distribution along the three axes of the body frame of the aircraft. This leads to three components of effective translational wind velocity and three components of effective rotational wind velocity. The effective rotational wind components are computed as

$$p_{\text{eff}} = \left(\frac{\partial W_z}{\partial y}\right)_{\text{eff}} - \left(\frac{\partial W_y}{\partial z}\right)_{\text{eff}} \tag{3}$$

$$q_{\text{eff}} = \left(\frac{\partial W_x}{\partial z}\right)_{\text{eff}} - \left(\frac{\partial W_z}{\partial x}\right)_{\text{eff}} \tag{4}$$

$$r_{\text{eff}} = \left(\frac{\partial W_y}{\partial x}\right)_{\text{eff}} - \left(\frac{\partial W_x}{\partial y}\right)_{\text{eff}} \tag{5}$$

C. Turbulence Modeling

Two methods of representing turbulence in a flight simulation are 1) a random velocity disturbance generated by filtered white noise shaped to a specific power spectrum, and 2) the use of natural turbulence recorded in wind tunnels or in the atmosphere [22]. Both of these methods are employed and compared in the simulation of the test flight. In the following discussion, u_g, v_g, w_g refer to the three components of the translational velocity turbulence, and p_g, q_g, r_g refer to the three components of the angular velocity turbulence.

1. Dryden Turbulence Model

As recommended in the military flying qualities specification, MIL-F-8785C [23,24], the Dryden power spectral density (PSD) functions are used to model turbulence as a stochastic process. The Dryden form of the spectra for the translational turbulence velocity components in the body frame of the aircraft is given in MIL-F-8785C [23]. The PSD functions are expressed in terms of Ω, the spatial frequency in radians per meter, σ_u, σ_v, σ_w, the rms turbulence intensities in meters per second, which are measures of the intensity of the turbulence, and L_u, L_v, L_w, the scale lengths in meters. MIL-F-8785C also provides the spectra for the angular velocity disturbance components in the body frame due to turbulence [23]. MIL-F-8785C [23] recommends the assumption of isotropy for turbulence above 20,000 ft, that is,

$$\sigma_u = \sigma_v = \sigma_w \tag{6a}$$

$$L_u = L_v = L_w \tag{6b}$$

To write the PSD functions $\Phi(\Omega)$ in terms of angular frequency ω in radians per second as $\phi(\omega)$, the following conversions are applied [25]:

$$\Omega = \frac{\omega}{V} \tag{7}$$

$$\phi(\omega) = \frac{\Phi(\Omega)}{V} \tag{8}$$

where V is the magnitude of the nominal airspeed of the aircraft.

In the MATLAB/Simulink implementation of the Dryden turbulence, Monte Carlo simulation [26] is used; that is, Gaussian white noise with unity spectral density is input to a linear filter for each component of translational and angular turbulence. Spectral factorization [27] is used to obtain the transfer functions and then state-space representations of the linear filters that yield signals with the Dryden power spectral densities. In the simulation, a band-limited white noise generator is used to obtain the zero mean Gaussian white noise with unity flat power spectral density. MIL-F-8785C [23] states that u_g, v_g, w_g, and p_g shall be considered mutually independent (uncorrelated) in a statistical sense, whereas q_g is correlated with w_g, and r_g is correlated with v_g. This is modeled in the simulation by using different seeds for the white noise generators of u_g, v_g, w_g, and p_g, whereas the seed of q_g is equal to that of w_g, and the seed of r_g is equal to that of v_g. Identification of the Dryden parameters to represent the turbulence experienced in the test flight is described in Sec. VI.

2. Use of Turbulence Data from Test Flight

As an alternative to the Dryden turbulence model, the turbulence can be extracted from the wind experienced by the receiver in the test flight. The turbulence extracted from the flight data will hereafter be referred to as "flight data turbulence." This approach has the advantage that it results from physical measurements and therefore should be the best representation of the actual turbulence experienced during the test flight. Section VI gives details of how the flight data turbulence is obtained.

D. Implementation of Wind Effects in the Six-Degrees-of-Freedom Dynamics Equations

In the aerial refueling simulation, the tanker is exposed to the prevailing wind and the Dryden model or flight data turbulence. The receiver is exposed to the same two wind sources, plus the wake-vortex-induced wind generated by the tanker. The sum of the wind sources for either aircraft is referred to as the total wind experienced by the aircraft. The total wind is incorporated directly into the nonlinear, 6-degrees-of-freedom (DOF) dynamics equations for both aircraft, as described in [9,11].

III. Description of the Test Flight

The AFRL AAR test flight was conducted over Lake Ontario, north of Rochester, New York, on 22 September 2004. A U.S. Air National Guard 107th Air Refueling Wing KC-135 was used as the tanker and a Calspan Learjet 25 was used as the surrogate receiver UAV. The test flight was conducted at a nominal altitude of 7010 m and with a nominal speed of 190 m/s. The receiver flew in formation with the tanker, alternating between the "observation" and "contact" flight positions. The observation position is the holding position taken by the receiver some distance away from the tanker, and the contact position is the position close to the tanker refueling boom to simulate aerial refueling. No physical contact was made between the receiver and the tanker during this test flight and no actual fuel transfer took place.

The tanker's calibrated airspeed from the air data avionics was recorded along with pressure altitude. Similarly, the receiver's avionics provided impact pressure, static pressure, and total temperature. Unlike the tanker, the receiver's instruments also provided the angle of attack, sideslip angle, and control surface deflections. Both aircraft were equipped with identical sets of GPS receivers, which were used for position and groundspeed measurements. Both aircraft were equipped with Litton LN-100 and LN-251 EGI (embedded GPS-inertial) units, where each provided a separate hybrid GPS-inertial navigation solution. The EGI units were used for acceleration, orientation, and body angular rates. Processing the flight data required consideration of multiple sample rates and time synchronization. These problems are fully addressed in [28].

Figure 4 shows the ground track of the tanker in terms of GPS latitude and longitude in degrees. While the tanker moves on this track, the receiver stays at the observation position or contact position relative to the tanker, or in transition between these two positions. Although different time clocks are used during data logging, all clock times recorded in the test flight were eventually converted to UTC (Coordinated Universal Time) in seconds, where 0 s is 22-Sept-2004 00:00 UTC. The numbers printed near the small squares on the tanker track in Fig. 4 indicate the start and end times of the observation and contact position passes. *Cx* and *Ox* indicate whether the receiver was at contact or observation position during the specific pass. There are two observation passes and four contact passes. The nominal observation position is (−59.13, 56.33, 0) m in the tanker's body frame. The nominal position for *C*1 is (−35.5, 2, 8.5) m, whereas the other three contact passes have the contact position aligned with the tanker centerline; that is, at (−35.5, 0, 8.5) m. Figure 5 shows the position of the receiver relative to the tanker in the UTC time domain. The vertical stripes indicate the time intervals when the receiver was at the observation or contact position. Note that start and end times of the stripes correspond to the UTC times printed in Fig. 4.

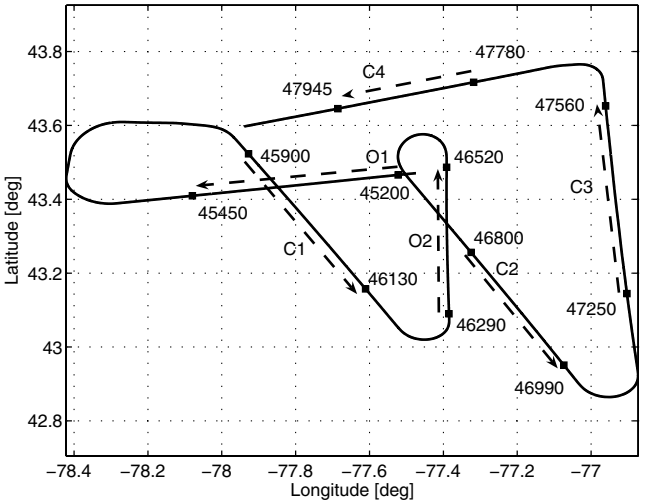

Fig. 4 Tanker GPS track with start and end times of observation and contact positions passes.

IV. Comparison of Tanker and Receiver Airspeeds

The true airspeed (VTAS) of the tanker and the receiver is calculated from the impact pressure, static air pressure, and total air temperature data using standard subsonic compressible flow equations [29,30]. Because both aircraft flew in formation through the same ambient air, the tanker's impact pressure was calibrated to match the receiver's impact pressure by subtracting 718.2 kPa. For complete details of the airspeed calculation, see [28].

Figure 6 shows the airspeeds of the tanker and receiver computed in the previous sections, as well as GPS-based speeds available from the flight data. A close examination shows that both aircraft have the same airspeed at observation 1. When the receiver goes to the contact position, the receiver airspeed decreases by roughly 1 m/s. The same observation can be made from the other observation and contact passes. Because the receiver aircraft is in the wake of the tanker when it is at the contact position, the decrease in the receiver airspeed at the contact position indicates the presence of vortex-induced wind that the receiver is exposed to whenever it is in the contact position. Further, comparison of the receiver or tanker airspeed with its own GPS-based speed in Fig. 6 reveals that, during the test flight, both aircraft were exposed to headwind or tailwind. When the airspeed is higher than the GPS-based speed (i.e., groundspeed), the aircraft are exposed to headwind. On the other hand, a lower airspeed is due to tailwind.

Figure 6 shows that 1) both aircraft were exposed to prevailing wind that switched between headwind and tailwind, 2) the receiver aircraft was exposed to additional wind when it was in the wake of the tanker, and 3) high-frequency oscillations in both tanker and receiver speeds indicate the presence of turbulence. In the next section, the wind velocities that the aircraft were exposed to will be quantified from the available flight data and the airspeeds computed in this section.

V. Calculation of Wind Components for Receiver and Tanker

The translational kinematics of an aircraft state that the velocity of an aircraft relative to an inertial frame is the sum of the velocity of the aircraft relative to the air and the velocity of the air relative to the inertial frame. This leads to an expression for the wind that the aircraft is exposed to

$$W_I = \dot{r}_B - \mathbf{R}_{\mathrm{BI}}^T \mathbf{R}_{\mathrm{BW}} [V \quad 0 \quad 0]^T \tag{9}$$

where W_I is the representation of the wind vector in the inertial frame, $\dot{r}_B$ is the representation of the aircraft's inertial velocity in the inertial frame, $\mathbf{R}_{\mathrm{BI}}$ is the rotation matrix from the inertial frame to the aircraft's body frame, $\mathbf{R}_{\mathrm{BW}}$ is the rotation matrix from the aircraft's

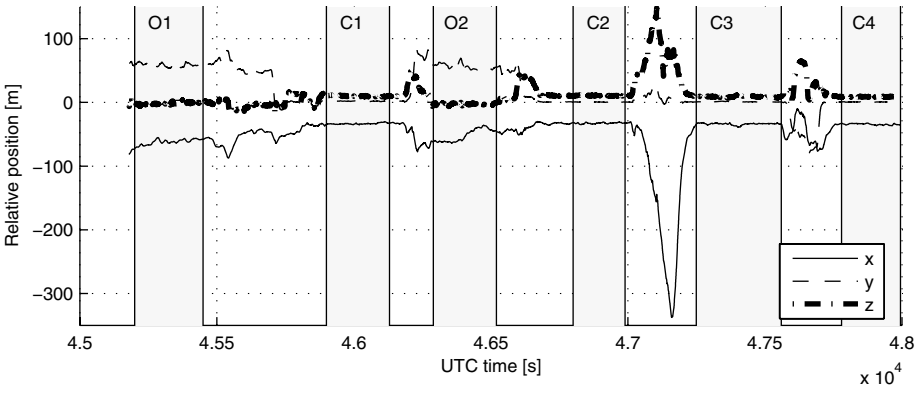

Fig. 5 Relative position from tanker c.m. to receiver c.m., written in the tanker's body frame.

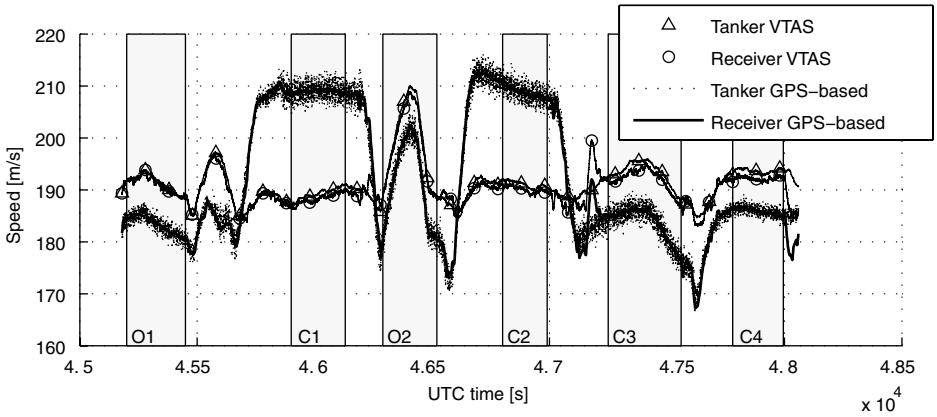

Fig. 6 Comparison of airspeeds and GPS-based speeds of tanker and receiver.

wind frame to body frame, and V is the aircraft's airspeed. Note that superscript T denotes the transpose of a matrix.

From the flight data, $\dot{r}_B$ is available as GPS-based and/or inertial measurement unit-based velocity measurement for both the tanker and the receiver, whereas V is the true airspeed computed in the previous section for both aircraft. The rotation matrix $\mathbf{R}_{\mathrm{BI}}$ can be expressed in terms of (ψ, θ, ϕ). Euler angles of both aircraft are available from their respective flight data. Similarly, rotation matrix $\mathbf{R}_{\mathrm{BW}}$ is expressed in terms of (β, α). Sideslip angle and angle-of-attack measurements of the receiver are also available in the flight data. However, the tanker's flight data do not provide these angles for the tanker. To be able to carry out the tanker's wind calculation in Eq. (9), it is assumed that the tanker's sideslip angle was zero and the angle of attack was equal to its pitch angle throughout the flight.

Figure 7 presents the results of Eq. (9) for both aircraft. The first observation from this figure, particularly from tanker-based results, is that, during the test flight, a prevailing wind was present with varying magnitude and direction relative to north and east directions. The down component of tanker-based wind shows a zero mean wind, which implies that no down/up draft as a component of the prevailing wind was present. The down component of receiver-based wind clearly shows the downdraft that the receiver experienced whenever it was in the contact position.

Figure 8 shows that the x component of the receiver-based wind is equal to that of the tanker when the receiver is at the observation position. When the receiver is at the contact position, the figure clearly shows that the x component of the wind experienced by the receiver is slightly higher (about 1 m/s). This implies that the

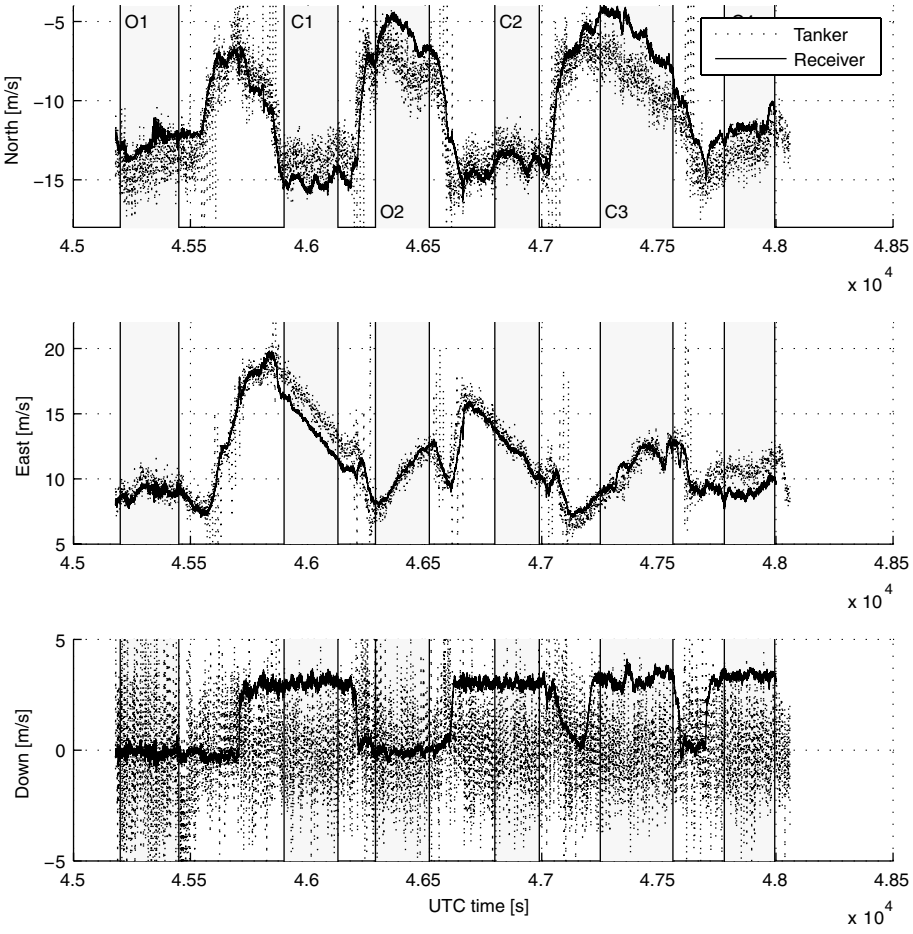

Fig. 7 Wind components in the inertial frame based on receiver and tanker data.

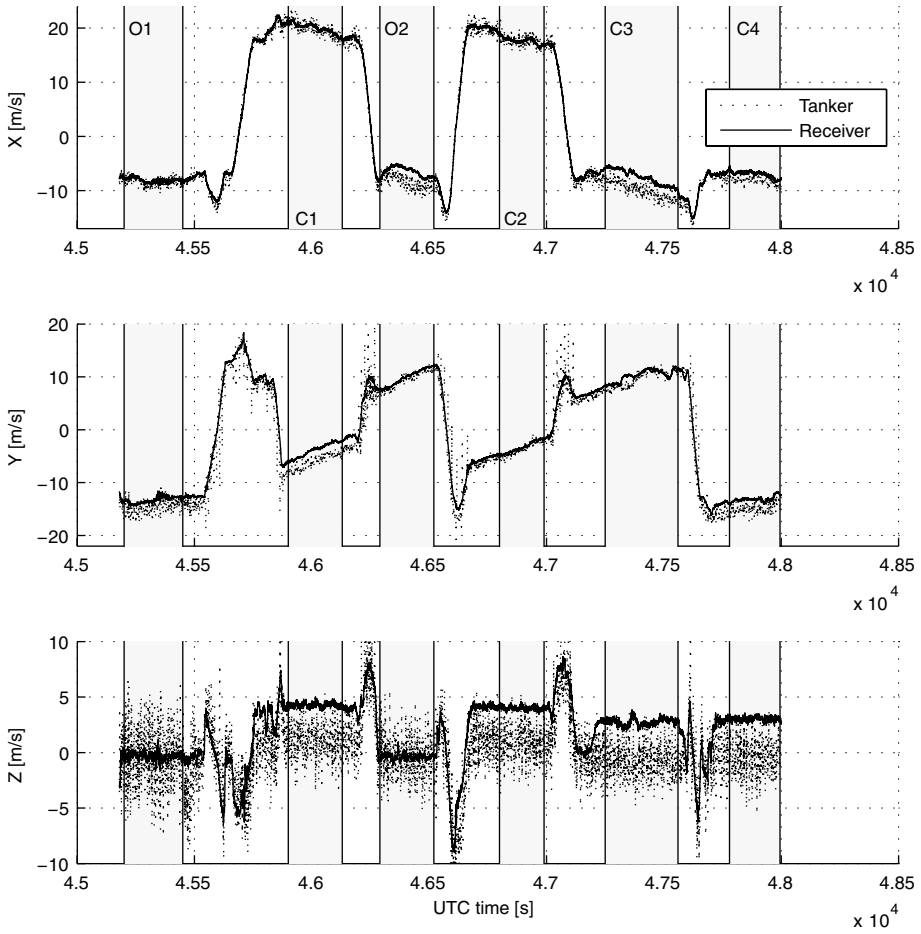

Fig. 8 Wind components in the receiver body frame based on receiver and tanker data.

tanker's wake-induced wind has a component in the positive x direction of the receiver, that is, wind component blowing toward the tanker. In the observation passes, the y component of receiver wind is slightly higher than that of the tanker. Because the receiver is outside the wake of the tanker when it is at the observation position, the receiver should not experience any additional crosswind. It was expected that both aircraft would have the same crosswind, as was the case in the x-wind analysis. The observed difference is attributed to possible errors introduced by sensor measurements and the assumption made for the sideslip angle and angle of attack in tanker's wind calculation. The difference becomes larger when the receiver goes to the first contact position from the first observation position. The increase is roughly 1.4 m/s. This observation implies that the receiver experiences sidewash induced by the wake vortex at the contact position. The difference is smaller at the second contact position and almost the same as that observed at the observation positions when the receiver was at the last two contact positions. The contact position $C1$ was offset from the centerline of the tanker, whereas the others were aligned with the centerline (noted in Sec. III). When the receiver is not aligned with the tanker centerline, it experiences sidewash induced by the tanker's wake-vortex system. This induced sidewash is manifested by the difference observed between the y components of the tanker and receiver winds.

As observed in Fig. 7, the third subplot in Fig. 8 also clearly shows the vortex-induced downwash that the receiver experiences when it is at the contact position. The magnitude of the downwash is 4 m/s at the first two contact positions and 3 m/s at the last two contact positions. From the first subplot of Fig. 8, it can be seen that, during the time of the first two contact passes, the aircraft were exposed to tailwind (wind in the positive x direction is tailwind) and, during the last two contact passes, the aircraft were exposed to headwind. As depicted in Fig. 9, with a positive pitch angle, tailwind resolved in the body frame has a component in positive z axis, whereas headwind

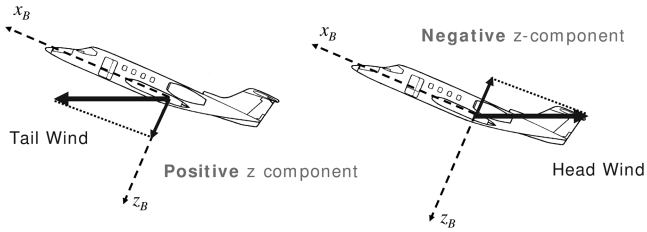

Fig. 9 Component of tailwind and headwind in body z axis.

has a component in negative z axis. The wind that the receiver experiences is the sum of the prevailing wind and the vortex-induced wind. Thus, prevailing tailwind increases the downwash effect, whereas prevailing headwind reduces it.

VI. Power Spectral Analysis of Receiver Wind Turbulence

In this section, an analysis is carried out on the frequency content of the components of the receiver wind through the PSD functions. This analysis is motivated by the fact that stochastic content of the atmospheric wind, that is, turbulence, is commonly modeled by PSD functions [23,24]. The mean variation of the receiver wind is attributed to the variations in prevailing wind and vortex-induced wind, both modeled as deterministic quantities. Thus, power spectral analysis is conducted on each wind component after subtracting the corresponding mean variation from the original signal. The mean variation of each wind component is calculated using a noncausal moving-window averaging filter:

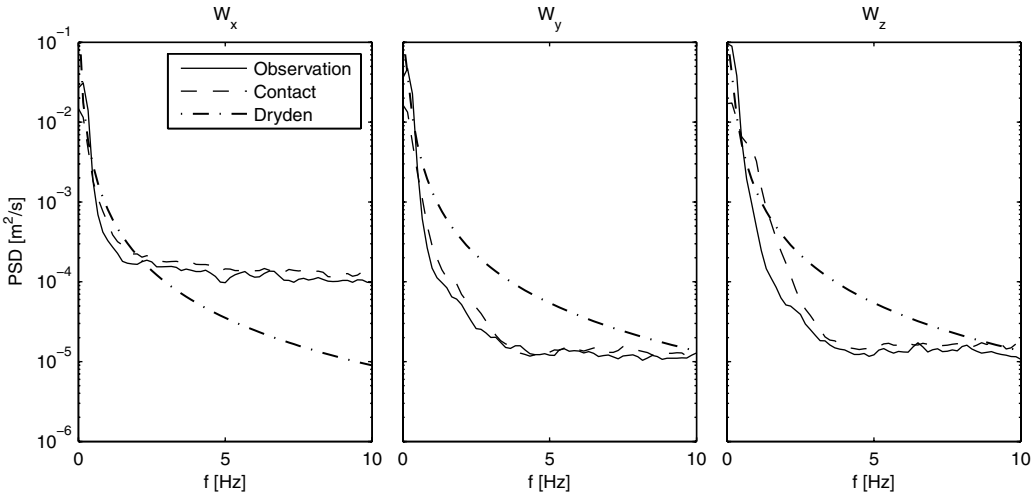

Fig. 10 PSD functions of receiver wind components. Comparison between observation and contact.

$$\overline{W}(k) = \frac{1}{2n+1}\sum_{i=k-n}^{k+n} W(i) \tag{10}$$

where $2n + 1$ is the window size and k is the discrete time index. [Equation (10) can also be used to calculate the mean variation of the tanker wind for use as the prevailing wind in the simulation, mentioned in Sec. II.] The PSD function of each wind component is based on the corresponding zero mean turbulence signal:

$$W_{\text{turb}} = W(k) - \overline{W}(k) \tag{11}$$

For the estimation of the PSD functions of W_{turb}, the Welch method [31] is used. Recall that there are two observation passes and four contact passes. Thus, for each component of the wind, two different PSD functions are computed: 1) based on two observation passes, and 2) based on four contact passes. A PSD function is calculated for each of the two observation passes, and then the average of the two PSD functions is called the PSD function based on two observation passes. Similarly, the four PSD functions are averaged for the contact passes. Figure 10 shows the two PSD functions for the x, y, and z components of the wind. For these 20 Hz signals, note that the PSD functions are plotted for the frequency up to 10 Hz, due to the Nyquist frequency at 10 Hz. The wind data show slightly more energy at contact position than that at observation position. However, the difference is so small that it is considered insignificant. Therefore, we conclude that the stochastic content of the wind is not influenced in a noticeable way by the wake vortices. Hereafter, the flight data PSD function is assumed to be the average of the observation and contact PSD in Fig. 10.

The signal W_{turb} can be used directly in the simulation as a turbulence source, as mentioned in Sec. II. Additionally, PSD functions of W_{turb} can be used to identify the parameters of the Dryden turbulence model. While flight data turbulence provides only the translational components (u_g, v_g, w_g), the Dryden model can also generate angular velocity turbulence (p_g, q_g, r_g). There are six parameters that can be varied among the translational and rotational turbulence PSD functions $(\sigma_u, \sigma_v, \sigma_w, L_u, L_v, L_w)$. To identify these parameters, the six parameters are varied to minimize the logarithmic least squares error, in the frequency range of 0 to 10 Hz, between the Dryden PSD functions and the PSD of the flight data turbulence from Eq. (11), according to the objective

$$\min_{\sigma,L}\sum_{f}[(\log\hat{\phi}_u - \log\phi_u)^2 + (\log\hat{\phi}_v - \log\phi_v)^2 + (\log\hat{\phi}_w - \log\phi_w)^2] \tag{12}$$

Here, ϕ is the true PSD from the flight data, $\hat{\phi}$ is the Dryden model PSD, and log is the base 10 logarithm. The logarithmic least-squares approach is taken to provide equal weight to the fit of the PSD over the whole frequency range, because the magnitude of the PSD function is a very small number at frequencies greater than about 0.5 Hz.

Parameter identification is performed under four sets of constraints on σ and L. The cases are summarized in Table 1. For the first three cases, the isotropic constraint is observed [Eq. (6)]. In case 1, L is fixed at 533.4 m, the value recommended by MIL-F-8785C [23]. In case 2, σ is fixed at 0.1 m/s, a representative value chosen for "light turbulence." The results of the parameter identification are shown in Table 2. Despite the large variations in the identified L, all of the sets of parameters in Table 2 produce similarly shaped PSD curves, differing mostly in the frequency range below 1 Hz. As a result, σ and L of case 1 are used in the rest of the analysis in this paper because this is the value of L recommended in MIL-F-8785C [23]. Figure 10 shows the resulting case 1 Dryden model PSD function and the receiver wind PSD functions. The turbulence level identified in case 1 is classified as light turbulence. This is because $\sigma = 0.37$ m/s (1.2 ft/s) at an altitude of 7000 m (20,000 ft) lies close to the "light" turbulence curve in the "RMS Turbulence Amplitude vs Altitude" figure in MIL-F-8785C [23]. This result is also consistent with what the pilots reported in the test flight.

VII. Simulation of Test Flight

The test flight is simulated with a MATLAB/Simulink model that includes tanker and receiver submodels. The tanker model is a nonlinear 6-DOF model of the KC-135, including wind effects. The tanker controller tracks commanded speed, altitude, and turn rate. Turn-rate scheduling is used to simulate the tanker motion from the test flight. The receiver model is a nonlinear 6-DOF model of the Learjet 25, including wind effects. The primary receiver controller,

Table 1 Dryden model parameter cases

Case 1	σ and L isotropic	σ varies, L fixed at 533.4 m
Case 2	σ and L isotropic	σ fixed at 0.1 m/s, L varies
Case 3	σ and L isotropic	σ and L both allowed to vary
Case 4	No isotropic constraint	All σ and L allowed to vary independently

Table 2 Dryden parameters from logarithmic least-squares fit (σ in m/s, L in m)

Case	σ_u	σ_v	σ_w	L_u	L_v	L_w
1	0.39	0.39	0.39	533.4	533.4	533.4
2	0.11	0.11	0.11	43.36	43.36	43.36
3	0.29	0.29	0.29	283.5	283.5	283.5
4	0.20	0.21	0.28	18.49	483.5	597.6

Table 3 Simulation cases

Simulation case	Turbulence source	Turbulence components	Receiver controller
1	Dryden model	u_g, v_g, w_g, p_g, q_g, r_g	controller 1
2	Dryden model	u_g, v_g, w_g	controller 1
3	Dryden model	u_g, v_g, w_g	controller 2
4	Flight data	u_g, v_g, w_g	controller 1

referred to as controller 1, tracks commanded position relative to the tanker. A commanded trajectory generation algorithm is employed, along with the position tracking controller, to simulate the Learjet 25 motion behind the KC-135. The second receiver controller, controller 2, is a speed, altitude, and turn-rate tracking controller similar to the tanker's controller. The second controller is used only to generate simulation data for analysis of the controller dynamics on the closed-loop response of the aircraft in terms of acceleration and angular velocity. For details of the controllers being employed, see [17,32].

The simulation is run to recreate the test flight. The simulated trajectory mirrors the actual test flight depicted in Fig. 4. The simulated trajectory slightly deviates from the test flight only during the turns. However, because the analysis focuses on the straight segments, this deviation is not important. To assess the two different turbulence generation methods and to investigate the effect of the controller on the PSD of the closed-loop response, four different simulation cases were run, as summarized in Table 3. In each case, a different combination of controller and turbulence source is used. The simulation results are analyzed in the next sections.

Figure 11 shows the components of the receiver position relative to the tanker from the flight test and simulation case 2. The positions at the contact and observation stations in the simulation are patterned after the actual relative position in the flight test. The maneuver from observation to contact involves three steps: 1) descend to the contact altitude, 2) move laterally to the position directly behind the tanker, 3) move forward to the final contact position. At the observation position, the receiver in the test flight deviates more from the nominal observation position than does the simulation. The simulation controller 1 performs better station keeping than the human pilot, at both observation and contact. A breakaway maneuver performed in the flight test can be seen between contact 2 and contact 3 in Fig. 11, where the receiver descends and falls behind several hundred meters. This maneuver is not performed in the simulation.

VIII. Analysis of Simulation Results and Comparison with Test Flight

A. Power Spectral Density Analysis

In this section, the PSD function is used to examine the effect of the turbulence model and the controller on the frequency response of the receiver. The simulation PSD is also compared with the flight data PSD to evaluate the performance of the simulation with respect to the test flight in the frequency domain. This analysis focuses on the closed-loop response of the receiver. The receiver acceleration and angular velocity is used to characterize the receiver's closed-loop response.

Figure 12 shows the PSD functions of the receiver acceleration in the x direction a_x for the observation and the contact position. The difference between observation and contact is negligible for this and the other aircraft state variables. For this reason, in the subsequent results, a PSD function from the simulation results is presented as a single curve, based on the average of the observation and contact positions.

The flight data turbulence is limited to the translational components (u_g, v_g, w_g) only. To make a direct comparison between

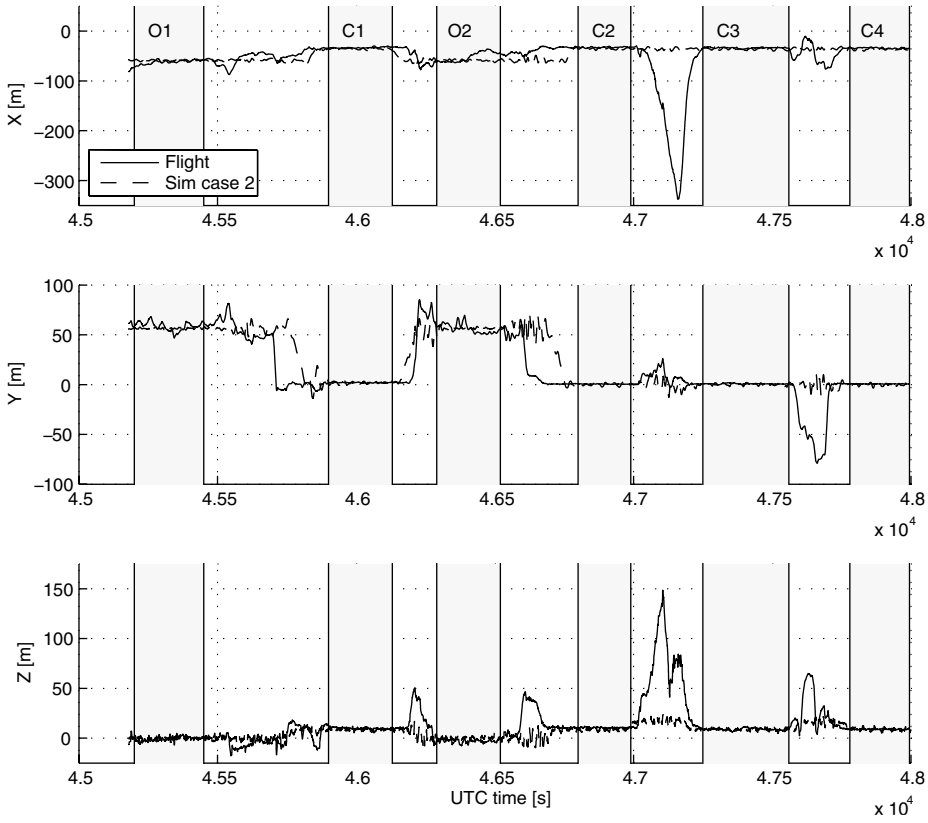

Fig. 11 Tanker-relative position time history from flight data and simulation case 2.

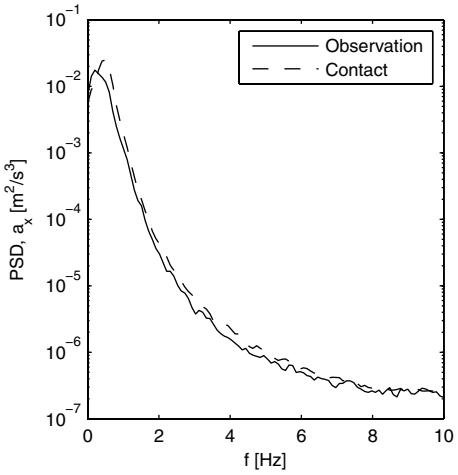

Fig. 12 PSD functions of the acceleration *x* component of the receiver from simulation case 1. Comparison between observation and contact positions.

the effect of the flight data turbulence and the Dryden model, the Dryden model must also be used with only the translational components; that is, with the rotational components (p_g, q_g, r_g) turned off. Investigations showed that the magnitude of the rotational turbulence components is negligible compared to the translational components, and that the simulation can safely be run using translational components only. For details of this investigation, see [28].

To compare the simulation results with the flight data, it is necessary to know the effect of the pilot or controller on the closed-loop response of the aircraft. Figure 13 shows the PSD functions for the receiver acceleration using the two receiver controllers. Although not presented here, angular velocity also has the same trend. In every case, the signals have more total power when the receiver uses controller 1, controlling the receiver position relative to the tanker. Qualitatively, tracking the commanded position relative to the tanker frame, which is accelerating and rotating, requires more control effort than maintaining altitude and speed. To deliver the required control authority of higher magnitude and frequency, controller 1 injects more energy into the system throughout the whole frequency range, resulting in the power increase in the PSD functions. This leads to an important observation: when examining the response of an aircraft to turbulence, the effect of the controller or pilot cannot be discounted. For this reason, direct comparisons between the frequency contents of flight data and the simulation data are not possible because, although the simulation attempts to model the turbulence in the actual test flight, no effort is made for the controllers in the simulation to represent the dynamic response of the pilot in the test flight.

With the preceding caveats, the simulation results can now be compared with the test flight data in the frequency domain to evaluate the simulation's performance. Figure 14 shows the PSD functions of the receiver acceleration and angular velocity from the simulation and the test flight. For the simulation curves, results are shown from

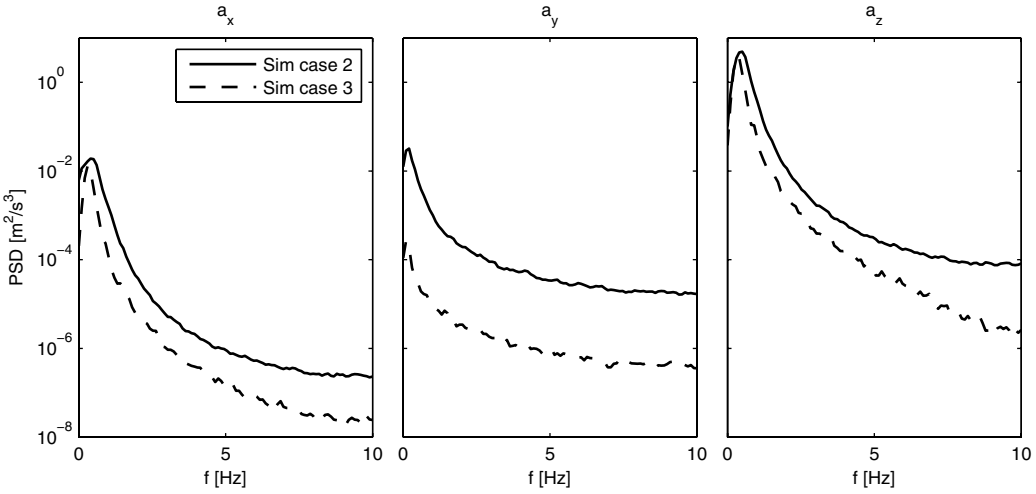

Fig. 13 PSD functions of the acceleration components of the receiver. Comparison between two different receiver controllers in the simulation.

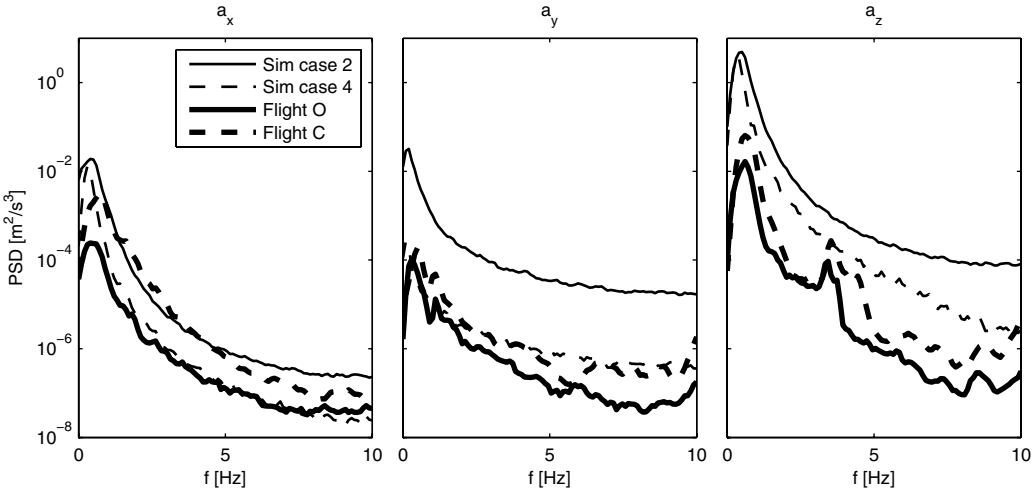

Fig. 14 PSD functions of the acceleration components of the receiver from the flight test data and the simulation.

cases 2 and 4, being with Dryden turbulence and with flight data turbulence, respectively. For the flight test curves, the observation and contact positions are shown. In general, all of the PSD curves rise to a peak value at a very low frequency near zero, and thereafter decrease until the Nyquist frequency. In contrast to the result shown in Fig. 12, there is a consistent and significant difference between the PSD functions for the observation and contact position in the flight data. There is always more power in the signals at contact compared to observation. By examining Fig. 13, the difference in power on Fig. 14 from observation to contact can be attributed to a change in the pilot's behavior. At the observation position, the pilot is not trying to strictly maintain a specific relative position from the tanker, and therefore his task is less demanding. At contact, the pilot must react and make changes to the aircraft position on a far tighter scale to maintain the appropriate position relative to the tanker. Further, the pilot has different visual cues at contact, which may require even more control effort. Therefore, the contact PSD of the aircraft response states is always higher than the observation PSD. The difference between the "relaxed" pilot at observation and the "stressful" pilot at contact is analogous to the difference between simulation receiver controllers 1 and 2. Although not presented, the angular velocity response also shows the same trend.

Figure 14 also shows the difference between the simulation results with the two turbulence sources. Angular velocity response, although not presented herein, also shows the same trend. In all cases, the Dryden model turbulence source produces a simulation result with more power than the flight data turbulence source. This suggests that the Dryden model parameter identification procedure described in Sec. VI results in stronger turbulence than the flight data turbulence. The differences can probably be explained by the differences in the flight test pilot and the controller used in the simulation, as well as shortcomings of the Dryden turbulence model and its parameter identification process. Additionally, the simulation does not have any sensor model: the flight data may be showing additional effects of sensor dynamics and noise.

B. Mean Variation Comparison

In this section, the mean variation of several receiver and tanker states are compared between the simulation results and the flight data. The mean variation comparison reveals the effect of the deterministic components of the wind modeling techniques: the prevailing wind and the trailing wake vortex. To make the mean variation as clear as possible, the signals in some of the following figures are smoothened using the moving average filter described in Eq. (10).

Figure 15 shows the angle of attack, sideslip angle, and pitch angle (α, β, θ) for the simulation and the test flight. At observation, the pitch angle is identical to the angle of attack. At contact position, the receiver pitches up from 2.5 to 3.5 deg, due to the presence of downwash behind the tanker. Note that the performance of the simulation matches the behavior observed in the test flight very well. This indicates the accuracy of the vortex model used in the simulation.

Figure 16 shows the receiver and tanker air and groundspeeds from the simulation. The same graph for the flight data is shown in Fig. 6. The same trend is observed in both the flight test and in the simulation. In the simulation, the airspeed of the receiver is the same as the tanker at the observation position. At the contact position, the receiver's airspeed is roughly 0.75 m/s lower than the tanker's due to the additional wind induced by the wake vortices of the tanker. Figure 16 can also be used for comparison of the receiver or tanker airspeed with its own inertial speed. Because the test flight prevailing wind profile is used in the simulation and the aircraft ground tracks in the simulation match the test flight well, the aircraft in the simulation experience exactly the same head and tail wind as in the test flight. The consistency of the simulation with the test flight in this regard can be seen by comparing Fig. 16 with Fig. 6.

Figure 17 shows the engine power used in the flight test and the simulation. For the test flight, the differential engine pressure is shown, which is an approximate measure of engine thrust. For the simulation, the throttle setting percentage is shown. In both the

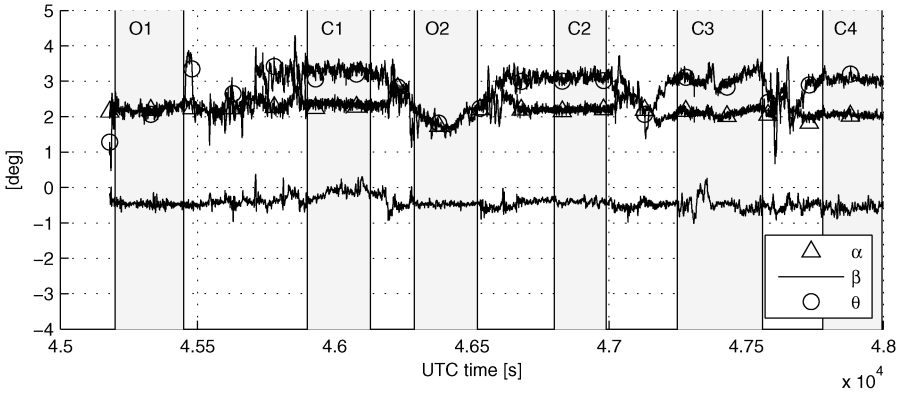

a) Flight data

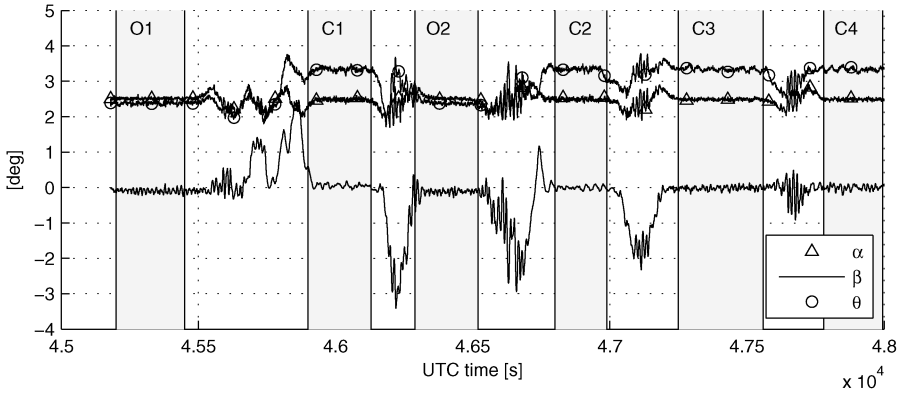

b) Simulation data, case 2

Fig. 15 Receiver angle of attack, sideslip angle, and pitch angle. Comparison between flight data and simulation.

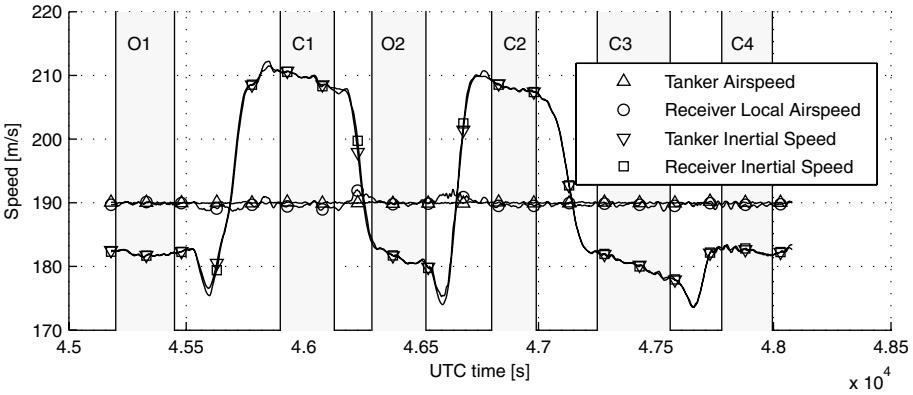

Fig. 16 Comparison of airspeeds and GPS-based speeds of the tanker and the receiver; simulation data, case 2.

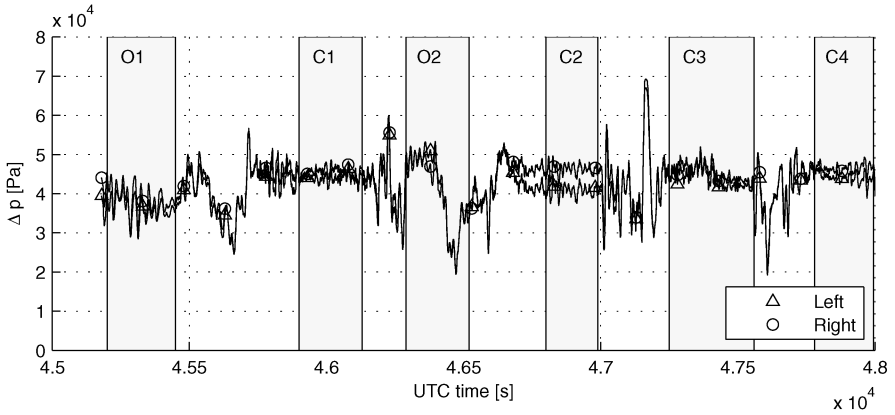

a) Receiver differential jet engine pressure, flight data

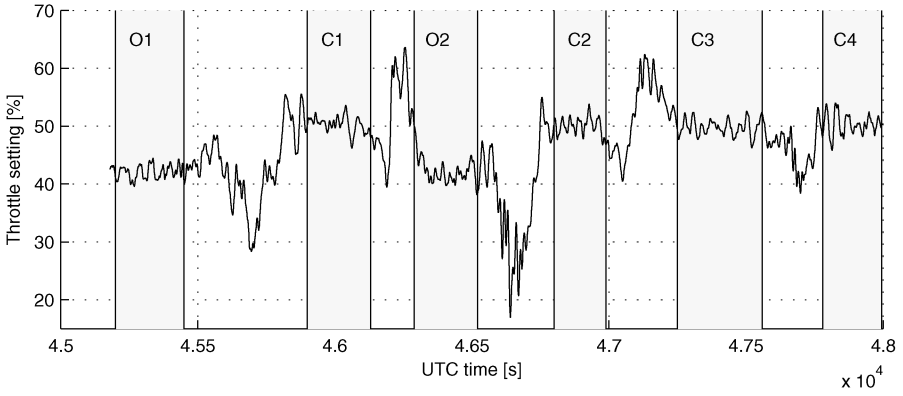

b) Receiver throttle setting; simulation data, case 2

Fig. 17 Comparison between receiver throttle setting for the flight data and the simulation results.

simulation and the test flight, the receiver at contact has to increase the engine power by about 20% to be able to maintain the relative position with the tanker while experiencing the vortex-induced wind.

Figure 18 shows the receiver wind in the receiver's body frame from the simulation. The same is plotted for the flight test in Fig. 8. In both the simulation and the flight, the tanker and receiver wind components in the x direction are the same at observation, but the receiver experiences, at the contact position, additional wind in the positive x direction (about 1 m/s), induced by the tanker's wake vortices. Recall that the vortex-induced sidewash on the receiver at the first contact position was identified from the flight data. The sidewash observed at the first contact position was not seen at the other contact positions. This was attributed to the lateral offset for the first contact position from the tanker centerline. In the simulation, the first contact position is also 2 m offset from the tanker centerline. The comparison of the difference in y components of the tanker and receiver winds when the aircraft are at observation 1 and contact 1 shows a similar trend. However, the magnitude of the sidewash in the flight is about 1.4 m/s, much larger than the 0.3 m/s in the simulation. This could be due to the presence of the refueling boom in the flight. The refueling boom, present in the flight but not modeled in the simulation, has lifting control surfaces that can induce additional sidewash in the flight that was not observed in the simulation. The sidewash can also be seen in the simulation in the y direction as the receiver moves laterally from observation to contact position, passing through the tanker vortex field. Note that, as the receiver moves closer to the tanker centerline, the magnitude of the sidewash decreases because the vortices from the left and right wing/tail reduce each other's effect.

The z-component plot in Fig. 18 shows the downwash that the receiver experiences in the simulation when it is at the contact position. The simulation result is in full agreement with the

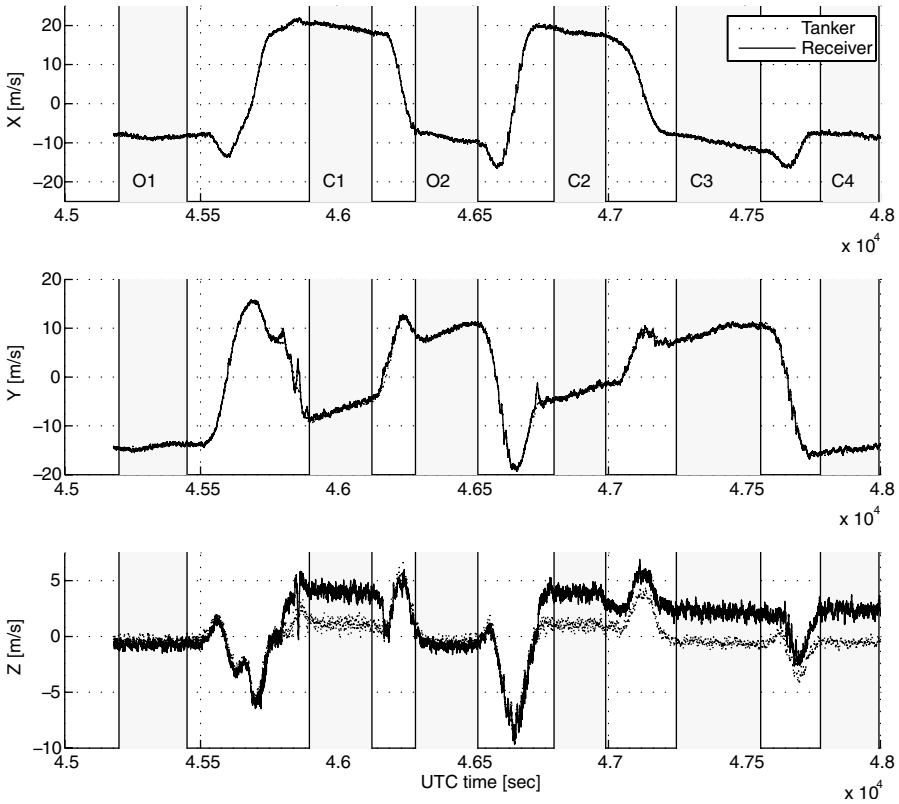

Fig. 18 Wind components in receiver body frame from simulation case 2.

downwash observed in the test flight (Fig. 8). At the first two contact positions, the downwash is 4 m/s, exactly the same as the test flight when the aircraft are exposed to tailwind. At the last two contact positions, when the aircraft are exposed to headwind, the downwash in the simulation is 2.5 m/s, very close to the test flight. The difference in the simulation results between the first two and last two contact positions, as explained in the test flight, is due to the prevailing wind being headwind or tailwind.

IX. Conclusions

Flight test data taken during a series of simulated aerial refueling maneuvers was analyzed. By manipulation of the existing air data measurements, the three components of the wind experienced by the tanker and receiver were separately identified. The effect of the induced winds from the tanker wake-vortex system is clearly seen by comparing these components. The stochastic turbulence was characterized by comparing the deviation of the wind components from their mean value. A power spectral density analysis was performed to identify the parameters used by the Dryden turbulence model. This analysis showed that the turbulence characteristics of the wind do not change when the receiver moves to the contact position in the wake of the tanker. A PSD analysis of the acceleration and the angular velocity measurements showed a clear power increase in the signals when the receiver was flown at the contact position. This is attributed to the higher pilot workload required to maintain the contact position directly below the tanker.

Six-degree-of-freedom simulations were conducted in an attempt to replicate the flight results. Two controllers, a position command system and a speed, altitude, and turn-rate tracker, were studied. Different combinations of Dryden and flight-based turbulence models were also studied. A conclusive comparison of the simulation with the flight data in the frequency domain cannot be done because the simulation used a controller that does not accurately model the pilot. Nonetheless, the frequency response of the aircraft was found to differ depending on the turbulence modeling technique used, and the acceleration and angular velocity responses in the simulation with the flight data turbulence appeared to be closer to PSD computed from the flight data than those with the Dryden model.

Comparison between the simulation and the test flight in the time domain was more definitive. The VEMT was found to accurately model the effect of the wake vortex on the dynamics of the receiver aircraft. The response of the receiver when it went to the contact position in the simulation was in perfect agreement with the flight data. The increase in the pitch angle and thrust, and the decrease in the airspeed at the contact position relative to the observation position, as observed in the test flight, were repeated in the simulation. The induced-wind components computed by VEMT in the simulation were also in agreement with those computed from the flight data. For example, the small decrease in the x component of the wind and the increase in the downwash when the receiver moved to the contact position were clearly seen in the simulation. The effect of the prevailing wind on the downwash as experienced by the receiver was also shown in the simulation. A prevailing tailwind had a positive contribution in the downwash when the receiver flies with a positive pitch angle, and vice versa. The prevailing wind also had an adverse effect on station-keeping performance. In the presence of a strong prevailing wind, station-keeping performance during turns differed depending on the direction the tanker turns relative to the wind. Although not directly observed in the flight data, the simulation results also showed the sidewash effect of the wake vortices, as well as the effective angular velocity of the air experienced by the receiver due to the induced nonuniform wind. This can be useful in explaining the response of the receiver moving behind the tanker in a test flight.

Acknowledgments

We would like to acknowledge the support of the U.S. Air Force Research Laboratory, Air Vehicles Directorate for this research. Atilla Dogan was supported as a Summer Faculty Researcher, and Timothy Lewis was supported as a Summer Graduate Student Researcher in the Control Design and Analysis Branch in Summer 2007, when this research was performed.

References

[1] Bloy, A., and Jouma'a, M., "Lateral and Directional Stability and Control in Air-to-Air Refueling," *Proceedings of the Institution of Mechanical Engineers, Part G: Journal of Aerospace Engineering*, Vol. 209, No. 4, 1995, pp. 299–305. doi:10.1243/PIME_PROC_1995_209_304_02

[2] Bloy, A., and Lea, K., "Directional Stability of a Large Receiver Aircraft in Air-to-Air Refueling," *Journal of Aircraft*, Vol. 32, No. 2, 1995, pp. 453–455. doi:10.2514/3.46741

[3] Pachter, M., Houpis, C., and Trosen, D., "Design of an Air-to-Air Automatic Refueling Flight Control System Using Quantitative Feedback Theory," *International Journal of Robust and Nonlinear Control*, Vol. 7, No. 6, 1997, pp. 561–580. doi:10.1002/(SICI)1099-1239(199706)7:6<561::AID-RNC291>3.0.CO;2-V

[4] Bennington, M. A., and Visser, K. D., "Aerial Refueling Implications for Commercial Aviation," *Journal of Aircraft*, Vol. 42, No. 2, 2005, pp. 366–375. doi:10.2514/1.4770

[5] Jewell, W., and Stapleford, R., "Mathematical Models Used to Simulate Aircraft Encounters with Wake Vortices," System Technology TR-1035-4 FAA Rept. DOT-FA73WA-3276-1, Aug. 1975, pp. 38–57.

[6] Pachter, M., D'Azzo, J., and Proud, A., "Tight Formation Flight Control," *Journal of Guidance, Control, and Dynamics*, Vol. 24, No. 2, 2001, pp. 246–254. doi:10.2514/2.4735

[7] Johnson, W., Teper, G., and Rediess, H., "Study of Control System Effectiveness in Alleviating Vortex Wake Upsets," *Journal of Aircraft*, Vol. 11, No. 3, 1974, pp. 148–154. doi:10.2514/3.60340

[8] Dogan, A., and Venkataramanan, S., "Nonlinear Control for Reconfiguration of Unmanned-Aerial-Vehicle Formation," *Journal of Guidance, Control, and Dynamics*, Vol. 28, No. 4, 2005, pp. 667–678. doi:10.2514/1.8760

[9] Dogan, A., Venkataramanan, S., and Blake, W., "Modeling of Aerodynamic Coupling Between Aircraft in Close Proximity," *Journal of Aircraft*, Vol. 42, No. 4, 2005, pp. 941–955. doi:10.2514/1.7579

[10] Venkataramanan, S., and Dogan, A., "Modeling of Aerodynamic Coupling Between Aircraft in Close Proximities," *Proceedings of the AIAA Atmospheric Flight Mechanics Conference and Exhibit*, AIAA Paper 2004-5172, Aug. 2004.

[11] Venkataramanan, S., and Dogan, A., "Dynamic Effects of Trailing Vortex with Turbulence and Time-Varying Inertia in Aerial Refueling," *Proceedings of the AIAA Atmospheric Flight Mechanics Conference and Exhibit*, AIAA Paper 2004-4945, Aug. 2004.

[12] Venkataramanan, S., and Dogan, A., "A MultiUAV Simulation for Formation Reconfiguration," *Proceedings of the AIAA Modeling and Simulation Technologies Conference and Exhibit*, AIAA Paper 2004-4800, Aug. 2004.

[13] Venkataramanan, S., Dogan, A., and Blake, W., "Vortex Effect Modelling in Aircraft Formation Flight," *Proceedings of the AIAA Atmospheric Flight Mechanics Conference and Exhibit*, AIAA Paper 2003-5385, Aug. 2003.

[14] Venkataramanan, S., and Dogan, A., "Nonlinear Control for Reconfiguration of UAV Formation," *Proceedings of the AIAA Guidance, Navigation, and Control Conference*, AIAA Paper 2003-5725, Aug. 2003.

[15] Venkataramanan, S., "Dynamics and Control of Multiple UAVs Flying in Close Proximity," M.S. Thesis, Univ. of Texas, Arlington, TX, July 2004.

[16] Dogan, A., Sato, S., and Blake, W., "Flight Control and Simulation for Aerial Refueling," *Proceedings of AIAA Guidance, Navigation, and Control Conference*, AIAA Paper 2005-6264, Aug. 2005.

[17] Dogan, A., Kim, E., and Blake, W., "Control and Simulation of Relative Motion for Aerial Refueling in Racetrack Maneuvers," *Journal of Guidance, Control, and Dynamics*, Vol. 30, No. 5, 2007, pp. 1551–1557. doi:10.2514/1.29487

[18] Tucker, J., Dogan, A., and Blake, W., "Derivation of the Dynamics Equations of Receiver Aircraft in Aerial Refueling," *Proceedings of the AIAA 45th AIAA Aerospace Sciences Meeting and Exhibit*, AIAA Paper 2007-251, Aug. 2007.

[19] Tandale, M. D., Bowers, R., and Valasek, J., "Trajectory Tracking Controller for Vision-Based Probe and Drogue Autonomous Aerial Refueling," *Journal of Guidance, Control, and Dynamics*, Vol. 29, No. 4, 2006, pp. 846–857. doi:10.2514/1.19694

[20] Pamadi, B. N., *Performance, Stability, Dynamics, and Control of Airplanes*, 2nd ed., AIAA, Reston, VA, 2004, Chap. 1.6.

[21] Thwaites, B. (ed.), *Incompressible Aerodynamics: An Account of the Theory and Observation of the Steady Flow of Incompressible Fluid Past Aerofoils, Wings, and Other Bodies*, Dover, New York, 1987, pp. 34–35.

[22] Etkin, B., "Turbulent Wind and Its Effect on Flight," *Journal of Aircraft*, Vol. 18, No. 5, May 1981, pp. 327–345. doi:10.2514/3.57498

[23] "Flying Qualities of Piloted Airplanes," TR MIL-SPEC MIL-F-8785C, 5 Nov. 1980.

[24] Moorhouse, D. J., and Woodcock, R. J., "Background Information and User Guide for MIL-F-8785C, Military Specifi- cation Flying Qualities of Piloted Airplanes," Interim Rept. for May 1977–1981, Air Force Wright Aeronautical Lab. TR-81-3109, Flight Dynamics Lab., Wright–Patterson AFB, OH, July 1982.

[25] McLean, D., *Automatic Flight Control Systems*, Prentice–Hall, Upper Saddle River, NJ, 1990, Chap. 5.

[26] Campbell, C. W., "A Spatial Model of Wind Shear and Turbulence for Flight Simulation," NASA, TR TP-2313, George C. Marshall Space Flight Center, AL, May 1984.

[27] Friedland, B., *Control System Design, An Introduction to State-Space Methods*, McGraw–Hill, New York, 1986, Chap. 10.

[28] Lewis, T. A., "Flight Data Analysis and Simulation of Wind Effects During Aerial Refueling," M.S. Thesis, Univ. of Texas, Arlington, TX, May 2008.

[29] Lan, C. E., and Roskam, J., *Airplane Aerodynamics and Performance*, Roskam Aviation and Engineering Corp., Ottawa, KS, 1988.

[30] Staff, A. R., "Equations, Tables, and Charts for Compressible Flow," NACA, TR 1135, Ames Aeronautical Lab., Moffett Field, CA, 1953.

[31] Stoica, P., and Moses, R., *Spectral Analysis of Signals*, Pearson Education, Upper Saddle River, NJ, Chap. 2.7.2.

[32] Kim, E., "Control and Simulation of Relative Motion for Aerial Refueling in Racetrack Maneuver," M.S. Thesis, Univ. of Texas, Arlington, TX, May 2007.